6-2016

On the Observability of Bottom Topography from Measurements of Tidal Sea Surface Height

Edward D. Zaron
Portland State University, ezaron@pdx.edu

Citation Details

Zaron, E. D. (2016). On the observability of bottom topography from measurements of tidal sea surface height. Ocean Modelling, 102, 55–63. http://doi.org/10.1016/j.ocemod.2016.04.008

Ocean Modelling 102 (2016) 55–63

Contents lists available at ScienceDirect

Ocean Modelling

journal homepage: www.elsevier.com/locate/ocemod

On the observability of bottom topography from measurements of tidal sea surface height

Edward D. Zaron

Department of Civil and Environmental Engineering, Portland State University, P.O. Box 751, Portland, OR 97207-0751, United States

ARTICLE INFO

Article history:
Received 10 December 2015
Revised 19 April 2016
Accepted 23 April 2016
Available online 26 April 2016

Keywords:
Data assimilation
Bottom topography
Tides

ABSTRACT

The question of whether features of the ocean bottom topography can be identified from measurements of water level is investigated using a simplified one-dimensional barotropic model. Because of the nonlinear dependence of the sea surface height on the water depth, a linearized analysis is performed concerning the identification of a Gaussian bump within two specific depth profiles, (1) a constant depth domain, and, (2) a constant depth domain adjoining a near-resonant continental shelf. Observability is quantified by examining the estimation error in a series of identical-twin experiments varying data density, tide wavelength, assumed (versus actual) topographic correlation scale, and friction. For measurements of sea surface height that resolve the scale of the topographic perturbation, the fractional error in the bottom topography is approximately a factor of 10 larger than the fractional error of the sea surface height. Domain-scale and shelf-scale resonances may lead to inaccurate topography estimates due to a reduction in the effective number of degrees of freedom in the dynamics, and the amplification of nonlinearity. A realizability condition for the variance of the topography error in the limit of zero bottom depth is proposed which is interpreted as a bound on the fractional error of the topography. Appropriately designed spatial covariance models partly ameliorate the negative impact of shelf-scale near-resonance, and highlight the importance of spatial covariance modeling for bottom topography estimation.

1. Introduction

Ocean bottom topography, i.e., the field of ocean depth relative to the undisturbed water surface, is a necessary component for the development of realistic ocean models. Topography influences ocean circulation at a wide range of spatial and temporal scales via kinematics, potential vorticity conservation, and through boundary layer processes. Gridded maps of ocean bottom topography are readily available to ocean modelers; however, their accuracy is poorly quantified (Marks and Smith, 2006) and the impact of topographic error on ocean forecasts is significant (Heemink et al., 2002; Blumberg and Georgas, 2008).

It is within this context that the problem of estimating bottom topography using data assimilation is studied here. The goal is to combine measurements of water surface elevation with hydrodynamic constraints in order to improve topographic maps, particularly on continental shelves where errors in gravimetrically-derived topography are large (Marks and Smith, 2012). The rationale for such an approach is provided by the observation that harmonic constants of the main diurnal (K_1) and semidiurnal (M_2) tides are known from satellite altimetry with 1cm precision, or better, over much of the ocean (Ray and Byrne, 2010; Stammer et al., 2014), which generally corresponds to a fractional error of 1–5%. The idea is that these data could be assimilated into an ocean tide model based on the Laplace Tidal Equations in which the bottom topography is treated as a distributed control parameter, and more accurate estimates of bottom topography could be obtained, particularly in regions where the relative uncertainty in the depth is greater than the relative uncertainty in the satellite-derived tides. This generic approach has been tried previously (Mourre et al., 2004), but generalizing and validating the approach more widely has proved challenging.

The present approach studies the bottom topography estimation problem in a maximally-simplified setting in order to understand the interplay between the dynamics, domain geometry, and data density. An idealized one-dimensional model consisting of shallow water flow over variable topography is used to examine these factors by using the same estimation technique concurrently implemented with more realistic models. Thus, the present paper examines the accuracy with which isolated perturbations to sea-floor

E-mail address: zaron@cecs.pdx.edu, ezaron@pdx.edu

http://dx.doi.org/10.1016/j.ocemod.2016.04.008

topography can be identified from measurements of water level alone. The tidal dynamics are approximated by a one-dimensional linear shallow water model. The novelty of studying this simple system is that it allows the nonlinearity connected with the undisturbed water depth to be exhibited, and it permits a more systematic exploration of parameter space than would be otherwise possible.

This paper is organized as follows. The following section describes how variational data assimilation may be applied to identify bottom topography in a one-dimensional wave equation. Following that, the observability of bottom topography is analyzed in two particular cases, (1) a topographic perturbation to a constant depth ocean, and (2) a topographic perturbation to a constant depth ocean adjacent to a near-resonant continental shelf. In Section 3 the observability is defined and quantified by a simple norm, and the observability of the topography is contrasted with the observability of the sea surface height for the constant depth case. This is followed, in Section 4, by an analysis of a near-resonant continental shelf. For both geometries the observability is described as a function of non-dimensional parameters of relevance to applications, namely, the ratio of the spatial data density to the topographic length scale, the ratio of the wavelength of the tide to the topographic length scale, and the ratio of the assumed correlation scale of the topography to the actual correlation scale.

2. A simple model for bottom topography estimation using variational data assimilation

Consider a model for tidal waves within a domain between $x = 0$, the "coastline," where the depth-integrated water transport, U, vanishes; and $x = L$, the "open ocean," where water elevation, η, is specified. Both U and η are taken as complex-valued functions of x, the complex harmonic constants at a given tidal frequency, ω, here equal to $2\pi/12.42\,\mathrm{h}^{-1}$, the main semi-diurnal tidal frequency. The hydrodynamics consist of the continuity and momentum equations,

$$-j\omega U + g H\eta_x + C_d u_f U/H = 0 \tag{1}$$

$$-j\omega\eta + U_x = 0 \tag{2}$$

$$H = H_0(x) + h(x), \tag{3}$$

where $j = \sqrt{-1}$, H is water depth, g is gravitational acceleration, C_d is the bottom drag coefficient, and u_f is a bottom friction velocity which may depend on x. The equations are supplemented by $H = H_0(x) + h(x)$ to emphasize that the bottom topography shall be taken as a control variable, with H_0 its first guess, and h a correction to be determined by data assimilation. The system represents a simplification of the full shallow water system in which bottom stress is linearized, water density is assumed constant, the advective nonlinearity is neglected, and quadratic nonlinearity involving η has been neglected. The specification of the equations is completed by the boundary conditions, $U(0) = 0$ and $\eta(L) = \eta_0$. In this one-dimensional setting the Coriolis term modifies the dispersion relation in a non-essential manner and so rotation is neglected.

The topographic estimation problem is posed in the language of variational state estimation, where the model state consists of (H, U, η). An estimate for the state is sought which is consistent with the dynamics specified above, where adjustments to the bottom topography, h, bring the modeled and observed values of η into agreement, allowing for measurement error. It is assumed that the expected value of h is zero and its spatial covariance is given by C_{HH}. For testing purposes, the true solution $(\widetilde{H}, \widetilde{U}, \widetilde{\eta})$ is known, and measurements of $\widetilde{\eta}$ are given, $d_i = \widetilde{\eta}(x_i) + \epsilon_i$, for $i = 1, \ldots, M$, together the variance of ϵ_i, σ^2, the measurement noise. The covariance C_{HH} shall be represented in terms of a variance, $\sigma_H^2(x)$, and a spatial correlation function, $c_{HH}(x, y)$, as

$$C_{HH}(x, y) = \sigma_H(x) c_{HH}(x, y) \sigma_H(y). \tag{4}$$

Particular models for the variance and correlation shall be discussed below.

The estimator for (H, U, η) is given by the minimizer of the objective function,

$$J(H, U, \eta) = \int_0^L \int_0^L h(x) C_{HH}^{-1}(x, y) h(y) dy dx + \sum_{i=1}^{M} |\epsilon_i|^2 \sigma^{-2}, \tag{5}$$

where the data error is given by $\epsilon_i = \eta(x_i) - d_i$, and $|\epsilon_i|^2 = \epsilon\epsilon^*$ is defined using the complex-conjugate of ϵ, indicated with the super-script *. Taking the variation with respect to (H, U, η) leads to the following system for the minimizer of J,

$$j\omega\mu + C_d u_f \mu/H - \zeta_x = 0 \tag{6}$$

$$j\omega\zeta - g(H\mu)_x = -\sum_{i=1}^{M} \delta(x - x_i)(\eta(x_i) - d_i)\sigma^{-2} \tag{7}$$

$$\lambda = -g\mu\eta_x^* + C_d u_f \mu U^*/H^2, \tag{8}$$

with boundary conditions $\mu(0) = 0$ and $\zeta(L) = 0$. The auxiliary variables $\mu(x)$ and $\zeta(x)$ are Lagrange multipliers associated with the equalities (1) and (2). The optimal estimate of topography, $H(x) = H_0(x) + h(x)$, is computed from H_0, $\lambda(x)$, the covariance function $C_{HH}(x, y)$, and $h(x)$ using the definition,

$$h(x) = \int_0^L C_{HH}(x, y) Re[\lambda(y)] dy, \tag{9}$$

where $Re[\,\cdot\,]$ denotes the real part of its argument.

The objective function is quadratic in h and ϵ_i, but non-quadratic in the variables, H, η and U. Nonlinearity is an important issue, but it will not be emphasized compared to the basic linear structure of the estimation problem. Instead, assume the solution consists of a small perturbation (H', U', η') to a basic state, $(\overline{H}, \overline{U}, \overline{\eta})$. Then the solution of equations (1)–(8) approximately satisfies,

$$-j\omega U' + gH'\overline{\eta}_x + g\overline{H}\eta_x' + C_d u_f U'/\overline{H} - C_d u_f \overline{U}/\overline{H}^2 H' = 0 \tag{10}$$

$$-j\omega\eta' + U_x' = 0 \tag{11}$$

$$H' = (H_0 - \overline{H}) + h'. \tag{12}$$

The topographic correction, $h' = \int_0^L C_{HH} Re[\lambda]$, is once again obtained from the first-order optimality condition for an extremum of $J(H, U, \eta)$ written in terms of the adjoint variables (λ, μ, ζ),

$$j\omega\mu + C_d u_f \mu/\overline{H} - \zeta_x = 0 \tag{13}$$

$$j\omega\zeta - g(\overline{H}\mu)_x = -\sum_{i=1}^{M} \delta(x - x_i)(\eta(x_i) - \eta_i)\sigma^{-2} \tag{14}$$

$$\lambda = -g\mu\overline{\eta}_x^* + C_d u_f \mu \overline{U}^*/\overline{H}^2, \tag{15}$$

with boundary conditions $\mu(0) = 0$ and $\zeta(L) = 0$. If the set, $(\overline{H}, \overline{U}, \overline{\eta})$, used for the linearization solves equations (1)–(3), then the expression for λ may be written as,

$$\lambda = -\mu^* j\omega\overline{U}/\overline{H}\left(1 + 2jC_d u_f/(\omega\overline{H})\right), \tag{16}$$

where the dependence of λ on the basic state fields $\overline{U}$ and $\overline{H}$ is exhibited.

3. Case 1: constant depth basic state

The model in this section consists of the dynamics introduced above within a bounded domain, from $x = 0$ to $x = L = 10^7$ m, in which the basic state for the linearization is constant depth, $\overline{H} = 4000$ m. The topographic perturbation to be identified, $\widetilde{h}(x)$, is a Gaussian bump of amplitude $\Delta H = 400$ m, centered at $x = 6 \times 10^6$ m. The degree of nonlinearity, $\Delta H/\overline{H} = 0.1$, is small enough that a linear analysis suffices to demonstrate the salient points. The wavelength of the M_2 tide, $L_\tau = 9 \times 10^6$ m, is slightly shorter than the domain. The open boundary condition is simply $\overline{\eta}(L) = 1$ m (i.e., a cosine of unit amplitude). The values of the drag coefficient and friction velocity are taken as constants, $C_d = 3 \times 10^{-3}$ and $u_f = 0.05$ m/s, resulting in a weakly damped system, $C_d u_f/(\omega\overline{H}) = 10^{-4}$.

An expansion in terms of so-called "representer functions" may be used to transform the system of coupled differential equations, (10)–(15), into a finite-dimensional linear system (Bennett, 1992; Wahba, 1990). Let $\{d_i\}$ denote the real-valued data vector, for $i = 1, \ldots, M$, which corresponds to the real and imaginary parts of $\widetilde{\eta}(x_i)$. The optimal estimate of (h', U', η'), denoted $(\widehat{h}, \widehat{U}, \widehat{\eta})$, can be written as a linear combination of M representer functions (h_i, U_i, η_i),

$$\widehat{h} = \sum_i \beta_i h_i \tag{17}$$

$$\widehat{U} = \sum_i \beta_i U_i \tag{18}$$

$$\widehat{\eta} = \sum_i \beta_i \eta_i, \tag{19}$$

where (h_i, U_i, η_i) solves the linear system (10)–(15) with the inhomogeneity, $\delta(x - x_i)$ or $j\delta(x - x_i)$, on the right-hand-side of (14), depending on whether the ith measurement corresponds to the real or imaginary part of $\widetilde{\eta}(x_i)$.

The real-valued coefficient vector $\beta = \{\beta_i\}$, for $i = 1, \ldots, M$, is found by solving the linear system,

$$(R + C_{\eta\eta})\beta = d', \tag{20}$$

where the elements of the $M \times M$ matrix R are $R_{i,j} = \eta_i(x_j)$, and the elements of the $M \times 1$ vector d' are $d'_i = d_i - \overline{\eta}(x_i)$. The $M \times M$ matrix C_{dd} is the data error covariance matrix, assumed to be diagonal, $C_{dd} = \sigma_\eta^2 I$, where $\sigma_\eta = 10^{-2}$m in the examples, below.

Because the optimal estimate is a linear combination of representer functions, one for each measurement, the representers for the topography, transport, and surface elevation (h_i, U_i, η_i), can be related to the Jacobian derivative, or sensitivity, of the optimal estimate to the observation at the ith location. Given a single measurement at x_i, for example, the field $\partial\widehat{h}/\partial d_i$ is simply proportional to h_i. The corresponding solutions of the adjoint equations (13)–(15), $(\lambda_i, \mu_i, \zeta_i)$, are equal to the Jacobian derivatives of the observed variables to the field, e.g., $\lambda_i = \partial\eta'(x_i)/\partial h'$, the so-called adjoint sensitivity. Thus, the representer functions and their adjoints will be shown below in order to interpret the observability of the fields.

The observability of the topography will be quantified in terms of an L^2 norm of the estimation error,

$$\epsilon_H^2 = \frac{\int_0^L (\widehat{h}(x) - \widetilde{h}(x))^2 dx}{\int_0^L \widetilde{h}(x)^2 dx} \tag{21}$$

where the true topography is $\widetilde{H}(x) = \overline{H} + \widetilde{h}(x)$. Similarly, the observability of sea surface elevation will be measured by,

$$\epsilon_\eta^2 = \frac{\int_0^L |\widehat{\eta}(x) - \widetilde{\eta}(x)|^2 dx}{\int_0^L |\overline{\eta} - \widetilde{\eta}(x)|^2 dx}, \tag{22}$$

where $\widetilde{\eta}$ is the η field obtained by solving (1)–(3) with $H(x) = \widetilde{H}(x)$.

Observability has been studied as a function of the following non-dimensional parameters:

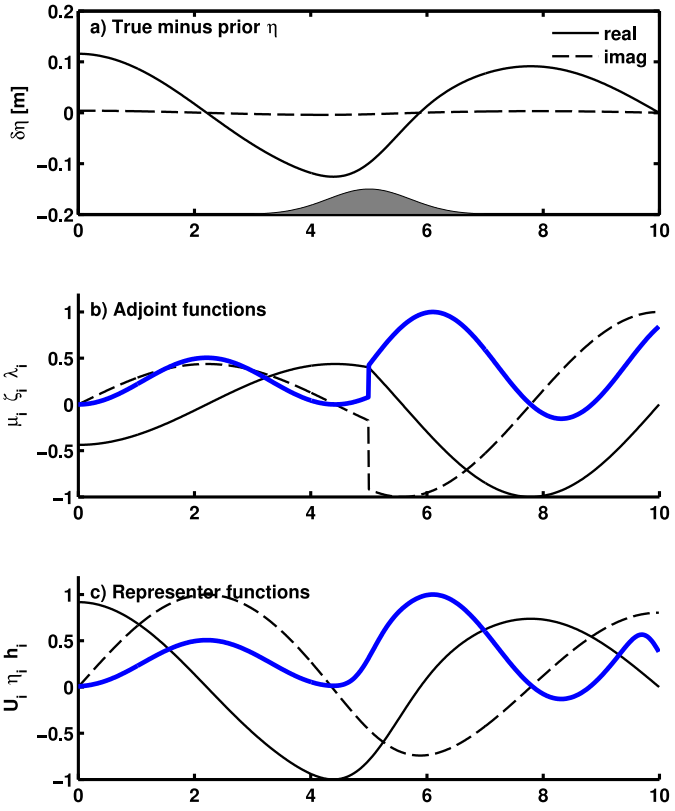

Fig. 1. Representative solutions for the flat-bottom case (x in units of 10^6 m). (a) The η field associated with the given topographic perturbation (shaded). (b) Selected real and imaginary parts of the adjoint functions, solutions to (13)–(15), for a measurement at $x_i = 5 \times 10^6$ m: real part of μ_i (dashed), imaginary part of ζ_i (solid), real part of λ_i (heavy). (c) Selected real and imaginary parts of the representer functions, corresponding to panel (b): imaginary part of U_i (dashed), real part of η_i (solid), real part of h_i (heavy).

- the spatial density of the data sites expressed as the ratio, D/L_c, where D is the separation between measurement sites (which are arranged evenly and sequentially within the domain), $D = x_{i+1} - x_i$, and L_c is the e-folding half-width of the Gaussian topographic bump;
- the ratio of the tide wavelength to the topographic perturbation width, L_τ/L_c, where $L_\tau = 2\pi\sqrt{g\overline{H}}/\omega$ is the wavelength of the tide;
- the ratio of the assumed width to the actual width of the topographic perturbation, $\widehat{L}_c/L_c$, where $\widehat{L}_c$ is the e-folding half-width of the correlation function c_{HH}; and
- the friction number, $r = C_d u_f/(\omega\overline{H})$.

Thus, D/L_c is a measure of the data resolution relative to the length scale of the unknown topography. L_τ/L_c is a measure of the dynamical scale of the topographic perturbation. $\widehat{L}_c/L_c$ is a measure of the accuracy of the spatial covariance model; note that $\widehat{L}_c/L_c = \sqrt{2}$ corresponds to perfect knowledge of the correlation scale. The friction number, r, determines the relative influence of the in-phase versus the quadrature components of $\overline{U}/\overline{H}$ on h, which roughly corresponds to the influence of $\overline{\eta}_x$ versus $\overline{U}$ (cf., Eq. (16)).

Within this section a homogeneous spatial covariance model is assumed,

$$\sigma_H(x) = \Delta H, \quad \text{and} \quad c_{HH}(x, y) = \exp(-(x - y)^2/\widehat{L}_c^2). \tag{23}$$

Fig. 1 illustrates the various fields for the given configuration. The basic state, $\overline{\eta}$, and true solution, $\widetilde{\eta}$, are both nearly sinusoidal standing waves and differ by roughly 0.1 m (Fig. 1a). The adjoint functions for a measurement at $x_i = 5 \times 10^6$ m are obtained

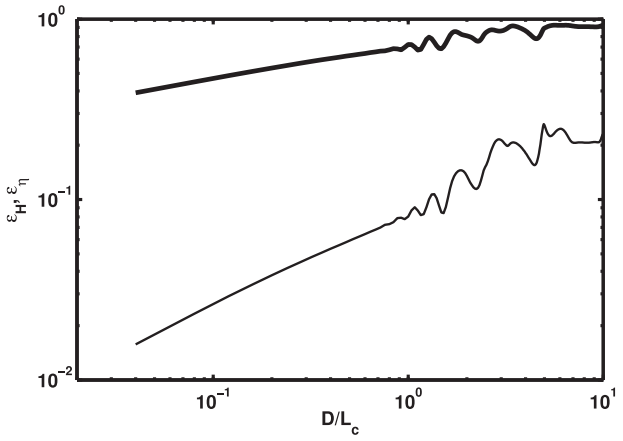

Fig. 2. Estimation error as a function of data spacing, D/L_c. The ϵ_H (thick) and ϵ_η (thin) functions are increasing functions of the data spacing, D/L_c, where D is the separation between the data sites and L_c is the width of the topographic perturbation. Errors fluctuate for $D/L_c > 1$ because of how the data sites sample the spatial variance of η.

by solving equations (13)–(15) with a unit delta function on the right-hand side of equation (14), $\delta(x - x_i)$. The solution contains a jump in the μ_i and λ_i fields, and a discontinuous derivative in the η_i field (Fig. 1b). The representer fields are obtained as the solution to (10)–(12), forced via the smoothed field $h_i = \int C_{HH}\lambda_i$ (Fig. 1c). Notice that the representer for the topography, $h_i(x)$, oscillates with approximately 1/2 the wavelength of the dynamical wave fields (η and U) because of its dependence on the product of μ and the physical fields. Because λ_i is discontinuous at the measurement site, the value of d_i is, in this case, correlated with the slope of the topography at that point.

The observability of η and H may be examined by considering how well the solution can be reconstructed from a given set of evenly-spaced measurements of η. The representer functions provide a basis for the space of all observable perturbations, and the functions ϵ_η and ϵ_H measure the efficiency with which a given set of measurements can determine the true η and H fields. Note that since the norm involved in ϵ_η and ϵ_H measures the deviation on the entire interval [0, L], and not just at the measurement sites, $\{x_i\}$, it is possible to over-fit the data at x_i resulting in a poor fit over the entire interval. Thus, the results shown depend the numeric value of σ_η, which controls the goodness-of-fit at $\{x_i\}$; although, the qualitative behavior is not sensitive to its precise value.

Fig. 2 presents ϵ_η and ϵ_H as a function of D/L_c. It is not surprising that η measurements are very efficient at observing η; even a single measurement of η is sufficient to reduce ϵ_η to less than 0.1. As more measurement sites are added and D/L_c is reduced, the value of ϵ_η is also reduced. The reduction is not monotonic since the particular locations of the data sites determine how well the peaks and troughs of the η field are sampled. For $D/L_c < 1$, the reduction of ϵ_η is essentially monotonic. In comparison, the observability of H is quite different. A data density of $D/L_c < 0.6$ is required to reduce ϵ_H below 0.5.

Why is H estimated so poorly compared to η? The representer function, η_i, in Fig. 1c is a smooth sinusoid, and the span of $\{\eta_i\}$ efficiently explains the smooth function, $\delta\eta = \widetilde{\eta} - \overline{\eta}$, shown in Fig. 1a. The h_i representer shown in Fig. 1c is also smooth, and one might expect the set $\{h_i\}$ to efficiently explain the topographic bump in Fig. 1a; however, this is not the case. The error in the estimated topography is shown in Fig. 3a for a case with $M = 250$ evenly-spaced measurements of η. The existence of the topographic bump is identified, but the amplitude and placement of the bump are in error.

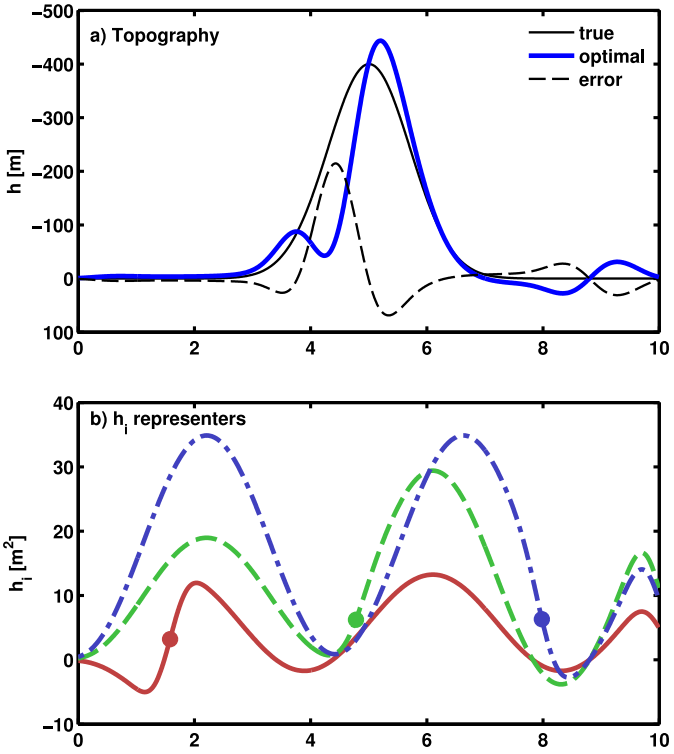

Fig. 3. Topography and representers. (a) The estimated topography (heavy line) is compared with the true topography (solid) and the error (dashed) when η observations are assimilated at $M = 250$ data sites. (b) The representer functions, $h_i(x)$, are shown at a subset of 3 of the M measurement sites. The measurement location, x_i, is shown with a dot.

To explain why the error in the topography is large on the left side of the bump, representer functions for 3 of the measurement sites are illustrated in Fig. 3b. The representers shown, and also those not shown, all have a small amplitude near the same location, $x = 4.5 \times 10^6$ m. Relative to other locations in the domain, all the h_i functions are inefficient at explaining variance near this site. The reason for this is the dependence of λ_i on the product, $\mu\overline{\eta}^*_x$, which is zero where the $|\eta|$ field has a local maximum, i.e., at the anti-amphidrome near $x = 4.5 \times 10^6$ m. In other words, the structure of the basic state $(\overline{H}, \overline{U}, \overline{\eta})$ determines the sensitivity of η to topographic perturbations, and the latter are essentially unobservable when they coincide with a local extremum of $|\overline{\eta}|$, where the magnitude of the gradient, $|\nabla\eta|$, is zero.

From now on the ratio $D/L_c = 0.1$ shall be kept fixed to examine the influence of the other parameters on a nominally well-resolved case.

The influence of the ratio of the dynamical wavelength to the topographic length scale, L_τ/L_c, is illustrated in Fig. 4. As previously, one observes that η is more observable than H, $\epsilon_\eta < \epsilon_H$. Several local extrema in the function $\epsilon_H(L_\tau/L_c)$ are labelled in the Figure; and, in certain cases (labelled 1, 2, 4, and 5), the topography becomes completely unobservable, e.g., near $L_\tau/L_c = 40, 12, 8, \ldots$. For these values of L_τ/L_c, the value of L_τ is such that the domain is near resonance, and miniscule changes in H lead to large changes in η; however, this extreme sensitivity near resonance also amplifies the errors in the linearized dynamics, making the linear estimator a poor estimate of $\widetilde{H}$.

It is not known if near-resonances will create the same difficulty for realistic applications in two-dimensions. In practice, the linear estimator is only used to identify the search direction in the function space of (H, U, η) (Zaron et al., 2011), so the impact of the amplified nonlinearity would be reduced. A realistic domain would

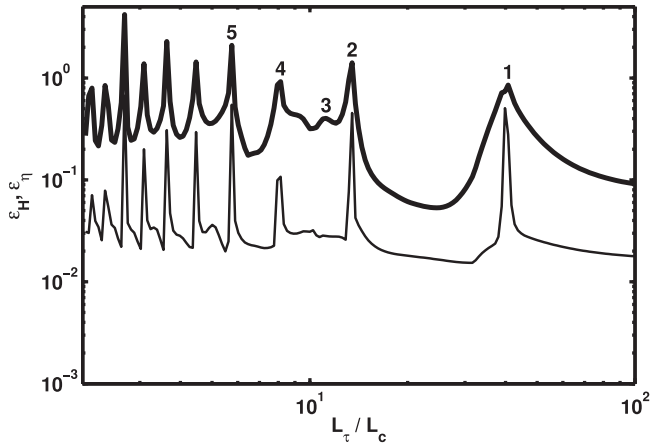

Fig. 4. Observability as a function of L_τ/L_c. The non-dimensional observability metrics, ϵ_H (thick) and ϵ_η (thin), are shown as a function of non-dimensional tidal wavelength, L_τ/L_c, where L_c is the width of the Gaussian bump and L_τ is the dynamical wavelength. The reduced observability of H near $L_\tau/L_c = 40, 12, 8, 5.5, \ldots$ (peaks labelled 1, 2, 4, 5) is caused by 1/4-wave resonance.

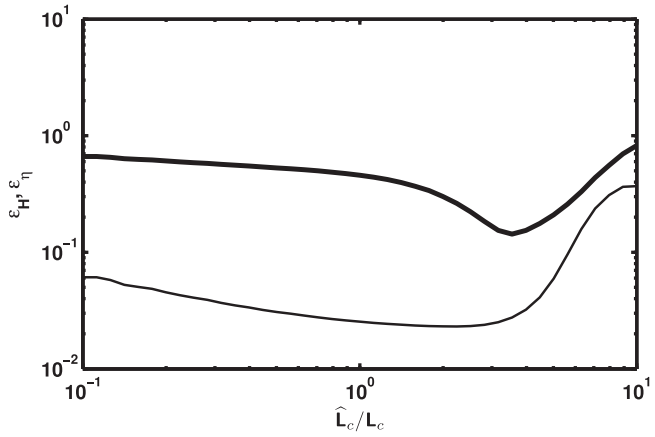

Fig. 5. Observability as a function of $\widehat{L}_c/L_c$. The non-dimensional observability metrics, ϵ_H (thick) and ϵ_η (thin), are shown as a function of the ratio the assumed to the actual topographic width scale, $\widehat{L}_c/L_c$. The observability of H is a weak function of $\widehat{L}_c$ so long as $\widehat{L}_c$ is smaller than about $3L_c$.

also contain topographic roughness which would further detune a resonance. Examination of the role of the nonlinearity in detail would require a global analysis, which is beyond the scope of the present work, but ignoring spikes caused by near-resonance, the over-all trend is for improved observability of H for larger L_τ/L_c (which also corresponds to increased data density relative the to spatial scale of the tide, L_τ/D). Beyond a certain point, though, the wavelength becomes so large that $\eta(x)$ is simply slaved to its open boundary value and it becomes insensitive to $H(x)$.

In practice the spatial correlation structure of the topographic perturbations is poorly known (Smith, 1993; Jakobsson et al., 2002). For the present calculation, the true topographic perturbation is characterized by a single length scale, L_c, and modeled with the length scale $\widehat{L}_c$. Fig. 5 illustrates the dependence of the observability functions on the ratio $\widehat{L}_c/L_c$, and shows that ϵ_H is insensitive to $\widehat{L}_c$ so long as $\widehat{L}_c/L_c < 3$. For larger values of $\widehat{L}_c$ the observability is degraded as the effective number of degrees of freedom are reduced. The influence of $\widehat{L}_c/L_c$ for values larger than 10 (not shown) is constrained by domain-size effects.

For the present case of a nearly constant depth domain, the influence of the friction number, r, on observability is very weak for $r < 1$ (not shown). For larger values of r the effects of damping lead to a boundary layer structure, with significant $|\eta|$ values re-

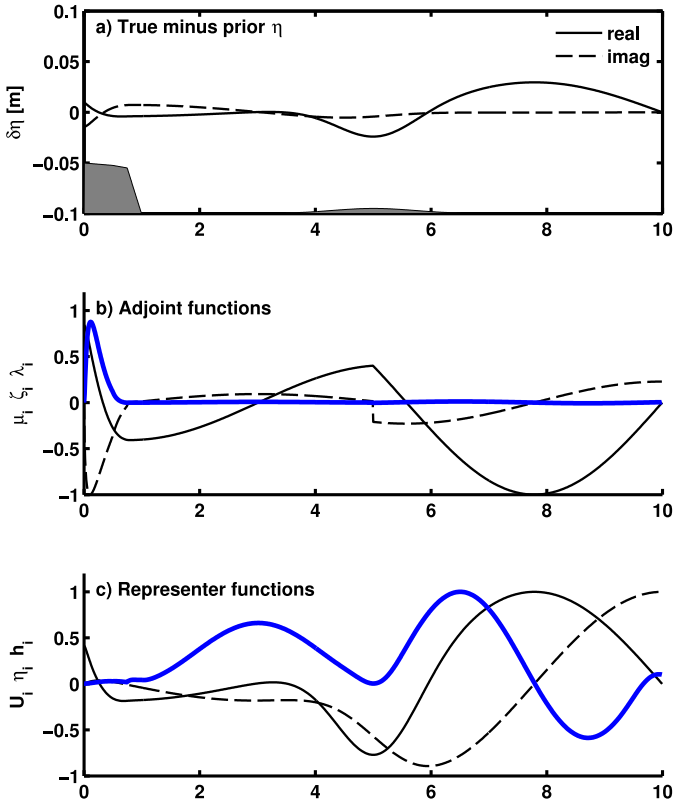

Fig. 6. Representative solutions for the near-resonant shelf case. (a) The η field associated with the given topographic perturbation (shaded). (b) Real and imaginary parts of the adjoint functions, solutions to (13)–(15), for a measurement at $x_i = 5 \times 10^6$ m: real part of μ_i (dashed), imaginary part of ζ_i (solid), real part of λ_i (heavy). (c) Real and imaginary parts of the corresponding representer functions: imaginary part of U_i (dashed), real part of η_i (solid), real part of h_i (heavy).

stricted to near the open boundary, $x = L$. In the present case the topographic bump is too far from the boundary to be of influence, and the topography becomes unobservable as r increases above 1.

4. Case 2: near-resonant shelf basic state

From the above discussion, it would appear that observations of surface elevation, $\eta(x_i)$, are sufficient to identify perturbations to the bottom depth with the caveat that the fractional error in H will be a factor of 10 or more larger than the fractional error in η. Thus, if the surface tide is known with a precision of $\epsilon_\eta = 10^{-2}$ (e.g., 1 cm precision for a 1 m amplitude tide), one might anticipate that under optimal circumstances the fractional error of the estimated topography will be $\epsilon_H = 10^{-1}$, or 10%. In sparsely sampled areas where uncertainty in topography exceeds 10%, this could represent a significant improvement.

Unlike the previous example, the real ocean is complicated by the presence of variable topography. In particular, continental shelves create spatially heterogeneous tides when near-resonances occur. The domain-scale resonances were problematic in the simple example, above, because the sensitivity of the linear system was amplified near resonance, and this led to the situation in which topography was essentially un-observable, as measured by ϵ_H^2. In the present case, with a near-resonant shelf embedded in a larger domain, it is found that the impact of near-resonant shelf is not restricted to the shelf, but it has a global impact on the estimated topography. The causes and consequences of this global impact are explained in this section.

Fig. 6 a illustrates the perturbation to η caused by the same topographic perturbation as considered previously, except that the

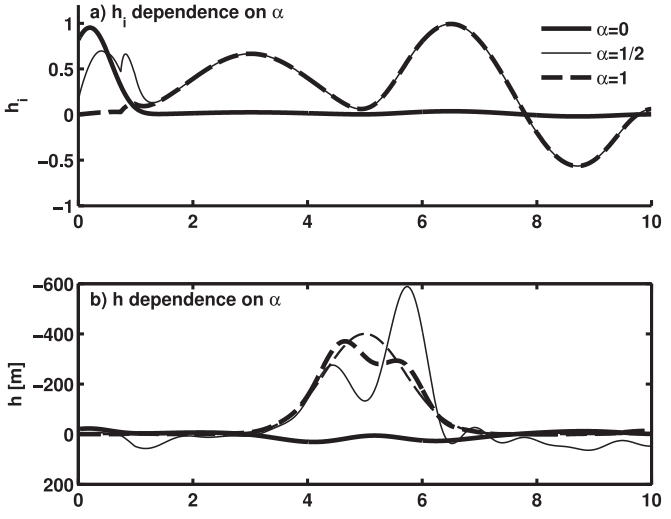

Fig. 7. Sensitivity to the topographic error scale parameter, α. (a) The influence of the topographic error model on the representer function, h_i, is shown for three values of α. The case $\alpha = 1$ corresponds to a constant fractional error in topography, which serves as a realizability condition in the limit $\overline{H} \to 0$. Note that the cases $\alpha = 1/2$ (thin line) and $\alpha = 1$ (thick dashed line) overlap in the domain interior ($x > 1.5 \times 10^6$ m). (b) The topography estimates corresponding to the α values in panel (a). The true topography is shown by the thin dashed line.

first guess topography, $\overline{H}$, contains a continental shelf. The topographic profile (shaded) represents a shelf from $x = 0$ to $x = l$, where $l = \pi\sqrt{gH_1}/(2\omega)$ is equal to 1/4 the wavelength of the tide for the depth $H_1 = 200$ m. The depth in the range of $x = 0$ to $x = l0^6$ m varies linearly from $\overline{H}(0) = 10$ m to $\overline{H}(l) = 200$ m, and this depth variation, combined with friction, detunes the resonance to a near-resonance. Note that the topographic perturbation centered at $x = 5 \times 10^6$ m is of the same form as used in Section 3; however, the vertical scale differs between Figs. 1 and 6.

The adjoint functions and representer functions, Fig. 6b and c, differ significantly from the corresponding functions in Fig. 1b and c. The largest values of λ_i and h_i occur over the continental shelf, $0 < x \leq l$, which indicates that the η function is most sensitive to small perturbations of the continental shelf topography. For essentially the same reason that the estimate of topography in the previous case was poor near $x = 4.5 \times 10^6$m (cf., Fig. 3), reconstruction of the topographic bump is impossible with the present setup.

But the relationship between h_i and λ_i is determined by the covariance function, C_{HH}, which is set a priori. Eq. (16) suggests that a realizability condition on C_{HH} might be necessary in order to prevent unrealistic (non-physical) divergence of the λ function near the coasts, in the limit $\overline{H} \to 0$. A sufficient condition to yield a physical solution in the limit of small $\overline{H}$ is that the covariance function behaves like $C_{HH}(x, y) \sim \overline{H}^{2\alpha}$, for some $\alpha > 1$, so that the product, $C_{HH}(x, y) \times (C_d u_f \mu \overline{U}^* / \overline{H}^2)$, is finite in the $\overline{H} \to 0$ limit. Given the representation in Eq. (4), the realizability condition may be expressed in terms of $\sigma_H(x)$ as $\sigma_H(x) \sim \overline{H}(x)^\alpha$. Note that $\alpha = 1$ corresponds to the condition that the fractional error in the topography is constant in the limit $\overline{H} \to 0$.

The influence of the parameter α is illustrated in Fig. 7a, where h_i is shown for three particular cases, $\alpha = 0$, 1/2, and 1. The case $\alpha = 0$ is repeated from above, and shows that all the spatial structure in h_i is confined to the shelf. The choice $\alpha = 1/2$ has structure both on the shelf and in the domain interior; however, the identification of the topographic bump is poor (Fig. 7b). The value $\alpha = 1$ greatly reduces the amplitude of h_i on the shelf, and it results in a satisfactory reconstruction of the topography.

From now on the value $\alpha = 1$ shall be used in the error model for the topography. The observability as a function of the density of

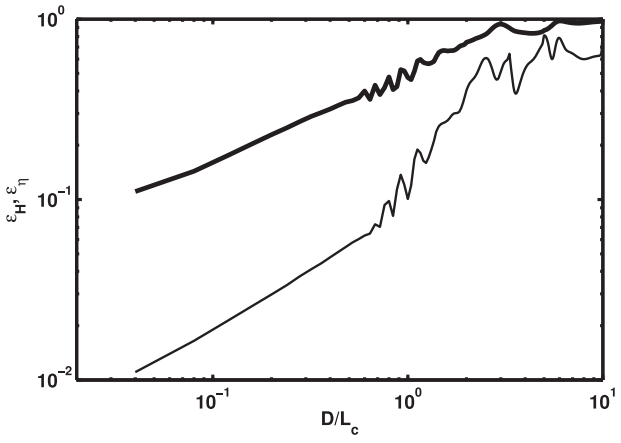

Fig. 8. Estimation error as a function of data spacing, D/L_c, for the near-resonant shelf case. Errors fluctuate strongly for $D/L_c > 0.6$ because of how the data sites sample the spatial variance of η, especially on the shelf.

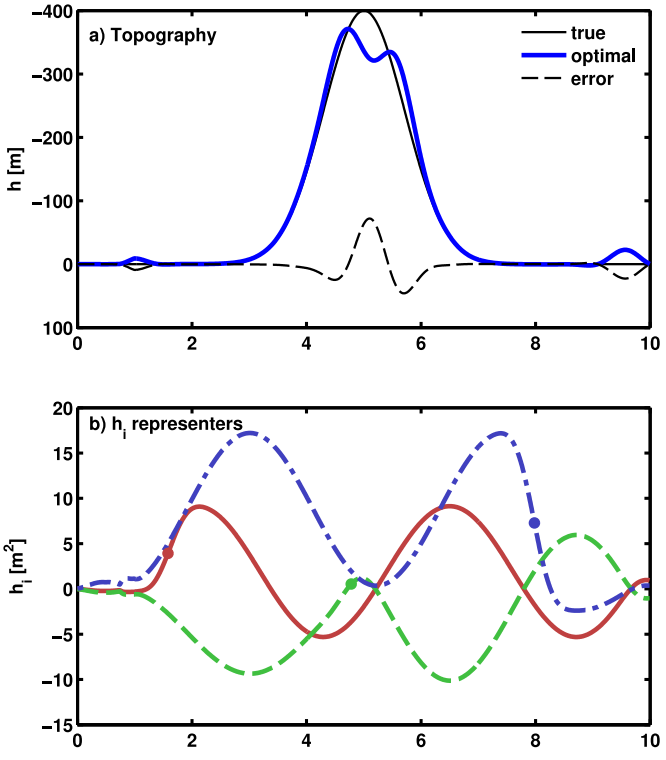

Fig. 9. Topography and representers. (a) The estimated topography (heavy line) is compared with the true topography (solid) and the error (dashed). (b) The representer functions, $h_i(x)$, are illustrated for x_i at a subset of 3 of the $M = 250$ measurement sites. The measurement location, x_i, is shown with a colored dot.

η observation sites is shown in Fig. 8. The situation is similar to the flat-bottom case (Fig. 2), except that higher density data is required before the monotonic convergence regime begins. The data density corresponds to the presence of 2-or-more η measurements on the continental shelf.

With 250 observation sites the main topographic bump is identified (Fig. 9); however, the estimation error is somewhat larger than in the previous case. Also, the spatial structure of h_i at the continental slope, near $x = 10^6$ m, has led to a spurious feature in the estimated topography, the magnitude of which is about 10% of the total depth at this site. This feature results from the form of the spatial covariance model, C_{HH}, which allows a correlation between the deep topography and that of the shelf and slope. It is

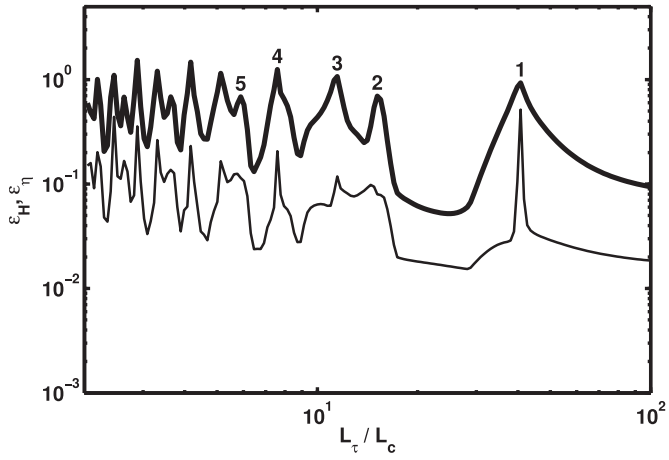

Fig. 10. Observability as a function of L_τ/L_c. Compare with Fig. 4.

is conceivable that this feature could be suppressed by a judicious choice of the correlation function, $c_{HH}(x, y)$, but this would require a non-stationary model for the spatial correlation. Identification of plausible models for the topography error is a subtle issue which shall be revisited later, in the Discussion.

The shelf case also shows additional complexity with regard to the ratio of the topographic and dynamical length scales, L_τ/L_c, where L_τ is the tidal wavelength in the deep water. The dependence illustrated in Fig. 10 is similar to Fig. 4 in that there are several local maxima in ϵ_H (labelled), associated with particular tidal wavelengths where the topographic bump becomes essentially unobservable. As in the flat-bottom case, most of these peaks (e.g., 1, 2, 4, and 5) are caused by a collapse of the dynamics and increased nonlinearity near resonance. The peak labelled 3 cannot be explained by resonance, and it requires further analysis to understand its cause.

In order to understand the lack of observability at near $L_\tau/L_c = 13$, it is helpful to consider the canonical decomposition of the representer matrix, $R = V\Sigma V^T$. The orthogonal matrix, $V = \{v_{ki}\}$, is comprised of basis vectors which may be interpreted as the spatial patterns of $\{\eta(x_i)\}$ variability which are most stably estimated by the observations. The basis vectors in V may be used to construct corresponding fields, denoted in bold, $\boldsymbol{\eta}_k$ and $\boldsymbol{h}_k$, called solution array modes (Bennett, 1992), which are linear combinations of the previously-mentioned representer functions,

$$\eta_k(x) = \sum_{i=1}^{M} v_{ki}\eta_i(x), \quad \text{and} \quad \boldsymbol{h}_k(x) = \sum_{i=1}^{M} v_{ki}h_i(x). \tag{24}$$

The solution array modes, $\{\boldsymbol{\eta}_k\}$ and $\{\boldsymbol{h}_k\}$ for $k = 1, \ldots, M$, form a (non-orthogonal) basis for observable η' and h' fields, respectively, the corrections to the first guess fields. Assuming that the singular values, $\sigma_k = \Sigma_{kk}$, are ordered as $\sigma_k > \sigma_{k+1}$, then the smaller k-modes (larger σ_k) are more stably estimated than the larger k-modes (smaller σ_k). The projection of the perturbation fields onto the dynamical array modes can be used to quantify how stably the given perturbations can be identified from observations.

With these definitions, it is possible to examine how the η' and h' project onto the solution array modes. The definition of a projection, $c(f, g)$, of function f onto function g is given by,

$$c(f, g) = \frac{\langle f, g\rangle}{\langle f, f\rangle^{1/2}\langle g, g\rangle^{1/2}}, \tag{25}$$

where $\langle f, g\rangle = \int |f(x)g^*(x)|dx$. Fig. 11 illustrates two cases identified from Fig. 12: a "best case" where $L_\tau/L_c = 22$, and a "worst case" where $L_\tau/L_c = 13$. In the best case (Fig. 11a) the perturbation η' (thin line) and h' (heavy line) fields both project primarily onto low modes which are stably estimated. In contrast, in the worst case (Fig. 11a), the perturbation η field projects uniformly onto the modes while the h field projects predominantly onto the higher modes which are less stably estimated. In other words, the particular configuration of the domain, tidal wavelength, and perturbation topography is such that η measurements provide an unstable and inaccurate estimate of the bottom topography.

To complete the comparison with the flat-bottom case, Fig. 12 illustrates the sensitivity of ϵ_η and ϵ_H to the ratio of the actual to assumed topography length scale. As was the case previously, the results show little sensitivity to $\widehat{L}_c$ so long as it is small enough. If $\widehat{L}_c$ is chosen too large, though, the ϵ_H error grows more rapidly than in the flat bottom case.

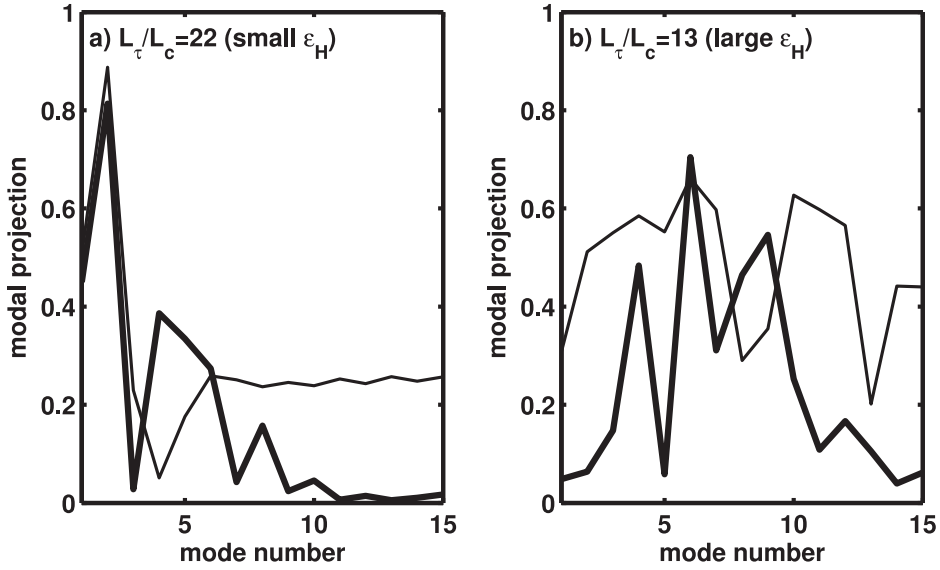

Fig. 11. Projection of the perturbations $\widetilde{\eta} - \overline{\eta}$ (thin line) and $\widetilde{h} = \widetilde{H} - \overline{H}$ (thick lines) onto the solution array modes for different values of L_τ/L_c. (a) In the best case (smallest ϵ_η) the perturbations project primarily onto the lowest modes. (b) In the worst case (labelled 3 in Fig. 10) η projects somewhat evenly onto the modes, but h projects more onto higher modes (up to mode 9). In other words $\widetilde{h}$ is projects onto a subspace that cannot be stably reconstructed.

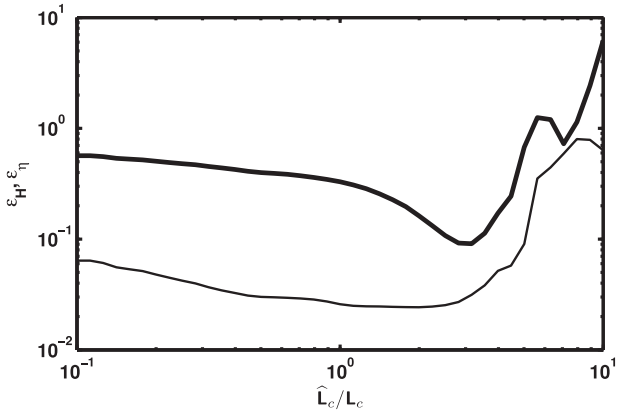

Fig. 12. Observability as a function of $\widehat{L}_c/L_c$. As in Fig. 5.

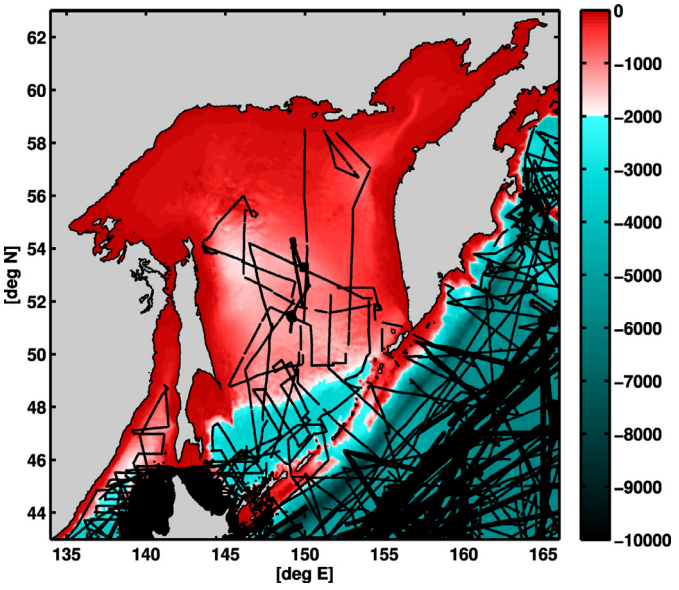

Fig. 13. Topography of the Sea of Okhotsk, as represented in version 15 of Smith and Sandwell (1997). Solid dots indicate locations of bathymetric data control points used to create the gridded topography.

5. Discussion

Due to its practical significance, the estimation or calibration of bottom topography in ocean models has a long history (Das and Lardner, 1991; Ten-Brummelhuis et al., 1993; Heemink et al., 2002; Losch and Wunsch, 2003; Mourre et al., 2004). The idealized model used here has permitted a systematic examination of the problem over an extensive parameter space. But what are the implications for less idealized applications of the methodology?

Consider the Sea of Okhotsk as a potential application where bathymetric measurements are sparse and contemporary gridded topographic maps differ significantly (Fig. 13). Relatively large tides in the Sea suggest favorable signal-to-noise for assimilation of altimeter-derived tides in order to improve the topography. Fig. 14 illustrates the locations of altimeter measurements where statistically independent estimates of tidal harmonic constants are available with an uncertainty of approximately 1.5 cm for the M_2 and K_1 tides. In mid-basin these uncertainties correspond to a fractional error of 3–5% in tidal elevation. Taking Figs. 2 and 8 as a guide, it appears that the error in topography inferred from these data ought to be in the 30–50% range at scales which are well-resolved by altimetry, say, 300 km. Intercomparison of existing gridded topographies indicates an uncertainty of 10–30% in this

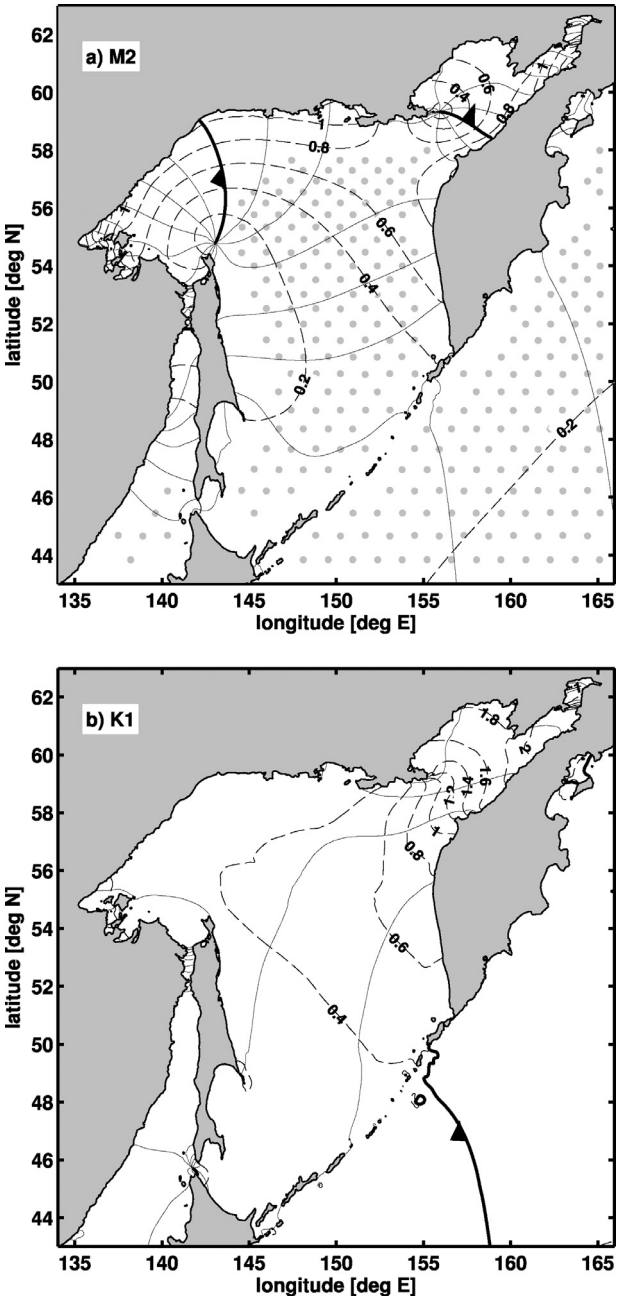

Fig. 14. Cotidal charts and locations of satellite altimeter data. (a) Locations of statistically independent estimates of the harmonic constants for the M_2 tide (gray dots), obtained by averaging multiple missions (TOPEX, JASON-1, and JASON-2; original and interleaved orbits). Solid lines indicate constant phase lines in 30° increments, and dashed lines indicate tidal amplitude (meters) with 0.2 m increment. (b) Cotidal chart for K_1.

region. Thus, it is hypothesized that incremental reductions in the topographic uncertainty should be achievable.

The idealized studies indicated that spurious topographic estimates might be obtained in two situations, (1) where the sensitivity of η to H is locally reduced because of the dependence of λ on $(\overline{H}, \overline{U}, \overline{\eta})$, especially at anti-amphidromes, and (2) where h cannot be stably estimated because of how the unknown topography projects onto higher-order solution array modes. Both cases ought to be identifiable by large a posteriori error estimates, i.e., by the sensitivity of the spurious features to slightly perturbed η measurements. From the cotidal charts for M_2 and K_1 in Fig. 14, one can infer a large range of $|\nabla\overline{\eta}|$ values; although, only one

unambiguous anti-amphidromic point is present, near 58°N–154°E for M_2. Because the anti-amphidromes of the diurnal and semi-diurnal tides do not, generally, coincide, the inclusion of data for multiple tidal constituents is warranted.

One final implication of the idealized experiments is the significance of the spatial covariance model for H errors. The topographic corrections are computed from the dynamically-derived sensitivity, λ, smoothed and scaled by the covariance C_{HH}. Unlike η, the topographic corrections are not directly constrained by measured values at the data sites; although measurements of H could certainly be assimilated in the present framework if they were available. Consequently, progress in the development of reliable models for the inhomogenous spatial covariance of gridded topographic data (Marks et al., 2010; Marks and Smith, 2012) will contribute to the success of the present approach.

6. Conclusions

An idealized model for the estimation of bottom topography from measurements of tidal water surface elevation has been investigated. There are many parameters which, in principle, determine the accuracy with which the topography may be identified, and the above analysis has focussed on a few non-dimensional parameters related to the length scale of the unknown topography and the wavelength of the tide, the latter being related to both its phase speed and frequency. The presence of nonlinearity in the dynamics when H is taken as a control variable led to the consideration of two specific cases for the first guess topography, and an elucidation of some domain size and configuration-dependent results. The results indicate that wave resonance may present an obstacle to identification of bottom topography. Near resonance the variance and parameter sensitivity are concentrated into a single mode, which leads to a reduction in the effective number of degrees of freedom, and an amplification of nonlinear effects. Whether near-resonance will present problems in realistic models has not been addressed, but it should be less problematic than in the one-dimensional case since realistic bottom roughness in $\overline{H}$ would allow for spatial damping and de-tuning of near-resonant geometries. Further work will be required to explore the nonlinear parameter space.

The sensitivity studies indicate that the fractional error in topography may be expected to be about 10 times larger than the fractional error in the water surface elevation. Excluding finite-domain-size and near-resonance effects, the bottom topography can be more accurately identified at scales small compared to the tidal wavelength, rather than at large scales, provided that the spatial density of data is sufficient to resolve the topographic features. Analysis of the assumed form of the topography error covariance model found significant sensitivity to the spatial variance model while the correlation length scale was less significant.

The present study used identical twin data assimilation experiments to analyze the observability of bottom topography in two particular cases. The estimation error that occurs when measurements are contaminated by inhomogeneous noise, as is always the case in practice, has not been addressed. The present analysis indicates that pathological cases can occur, even for smooth and well-resolved topography, where the surface elevation may be stably estimated but the estimated bottom topography may be unstable and inaccurate. Fortunately, the canonical decomposition used to study the situation here could also be applied in cases of practical interest, and the instability ought to be identifiable from small sample size Monte Carlo estimates of a posteriori errors.

Two factors have been identified which could lead to stable, but erroneous, estimates of topography. The first factor is the nonlinear dependence of the estimated topography on the first guess fields (cf., Fig. 3a near $x = 4 \times 10^6$ m, and Fig. 9a near $x = 5.5 \times 10^6$ m). In this weakly damped case, the product $\mu\overline{\eta}_x^*$ in (15) leads to an inability to estimate topographic perturbations in regions where there is no gradient in $\overline{\eta}$. The second factor concerns the spatial heterogeneity of the topography covariance model (cf., Fig. 9a near $x = 1 \times 10^6$ m). A realizability condition on the topography variance, σ_H^2, was suggested that is equivalent to a spatially-constant fractional topography error, but even with this condition, some adjoint sensitivity contaminated the topography estimate in the deep water near the shelf break. The large sensitivity on the shelf was a consequence of the near-resonant topography, $\overline{H}$, a phenomenon which is not uncommon in the world's oceans, and covariance modeling is likely to present significant difficulties in realistic applications.

Acknowledgment

The comments of two anonymous reviewers helped to improve the organization and clarity of this manuscript, and their contributions are appreciated. Support for this work was provided by the NASA Ocean Surface Topography Science Team, award number NNX13AH06G. Satellite altimeter data used in Fig. 14 were extracted from the RADAR Altimetry Database System (http://http://rads.tudelft.nl/rads/rads.shtml).

References

Bennett, A.F., 1992. Inverse Methods in Physical Oceanography, 1st edition Cambridge University Press, New York.
Blumberg, A.F., Georgas, N., 2008. Quantifying uncertainty in estuarine and coastal ocean circulation modeling. J. Hydraul. Eng. 134 (4), 403–415.
Das, S.K., Lardner, R.W., 1991. On the estimation of parameters of hydraulic models by assimilation of periodic tidal data. J. Geophys. Res. 96, 15187–15196.
Heemink, A.W., Mouthaan, E.E., Roest, M.R., Vollebregt, E.A., Robaczewska, K.B., Verlaan, M., 2002. Inverse 3D shallow water flow modeling of the continental shelf. Contin. Shelf Res. 22, 465–484.
Jakobsson, M., Calder, B., Mayer, L., 2002. On the effect of random errors in gridded bathymetric compilations. J. Geophys. Res. 107 (B12), 2350.
Losch, M., Wunsch, C., 2003. Bottom topography as a control variable in an ocean model. J. Atm. Ocean. Technol. 20, 1685–1696.
Marks, K., Smith, W., Sandwell, D., 2010. Evolution of errors in the altimetric bathymetry model used by Google Earth and GEBCO. Mar. Geophys. Res. 31, 223–238.
Marks, K.M., Smith, W.F., 2006. An evaluation of publicly available global bathymetry grids. Mar. Geophys. Res. 27, 19–34.
Marks, K.M., Smith, W.H., 2012. Radially symmetric coherence between satellite gravity and multibeam bathymetry grids. Mar. Geophys. Res. 33 (3), 223–227.
Mourre, B., De Mey, P., Lyard, F., Le Provost, C., 2004. Assimilation of sea level data over continental shelves: an ensemble method for the exploration of model errors due to uncertainties in bathymetry. Dyn. Atmos. Oceans 38, 93–121.
Ray, R.D., Byrne, D.A., 2010. Bottom pressure tides along a line in the southeast Atlantic Ocean and comparisons with satellite altimetry. Ocean Dyn. 60, 1167–1176.
Smith, W.H., 1993. On the accuracy of digital bathymetric data. J. Geophys. Res. 98 (B6), 9591–9603.
Smith, W.H., Sandwell, D.T., 1997. Global sea floor topography from satellite altimetry and ship depth soundings. Science 277, 1956–1962.
Stammer, D., Ray, R.D., Andersen, O.B., Arbic, B.K., Bosch, W., Carrére, L., Cheng, Y., Chinn, D.S., Dushaw, B.D., Egbert, G.D., Erofeeva, S.Y., Fok, H.S., Green, J.A.M., Griffiths, S., King, M.A., Lapin, V., Lemoine, F.G., Luthcke, S.B., Lyard, F., Morison, J., Müller, M., Padman, L., Richman, J.G., Shriver, J.F., Shum, C.K., Taguchi, E., Yi, Y., 2014. Accuracy assessment of global barotropic ocean tide models. Rev. Geophys. 52 (3), 243–282.
Ten-Brummelhuis, P.G., Heemink, A.W., van den Boogard, H., 1993. Identification of shallow sea models. Int. J. Num. Methods. Fluids 17, 637–665.
Wahba, G., 1990. Spline Models for Observational Data. SIAM publications, Philadelphia.
Zaron, E.D., Pradal, M., Miller, P.D., Blumberg, A.F., Georgas, N., Li, W., Cornuelle, J.M., 2011. Bottom topography mapping via nonlinear data assimilation. J. Atm. Ocean. Technol. 28, 1606–1623.